



Stability and strength behavior of thin-walled roof-panel-purlin system under wind loading

Yared Shifferaw¹, Kermelos Woldeyes², Girma Bitsuamlak³

Abstract

The objective of this paper is to examine the stability and strength behavior of trapezoidal thin walled steel roof panel-purlin systems under the action of realistic spatial wind loading. The current practice of applying uniform static pressure to test the effect of wind loading on thin walled metal roof panels fails to capture the realistic representation of wind effects. The trapezoidal roof panel-purlin system is examined for wind loading by adopting pressure coefficient readings from wind tunnel tests conducted at the University of Western Ontario for a low-rise building. Computational fluid dynamics model is developed and validated, with simulations used to generate more refined spatially-varying wind loading. Finite element analysis is undertaken to carry out the stability analysis of the roof model where buckling loads and modes are compared with results from uniform uplift pressure tests. A comparative study is conducted for examining the stability and strength of Z-section purlins due to cross-sectional distortion induced by wind-uplift under current design assumptions and realistic wind loading. In addition, parametric studies examining the stability of the thin-walled roof panel-purlin system for imperfection sensitivity and impact on distortional buckling due to the wind-uplift direction and associated fastener pull-out are conducted. The collapse behavior of the panel-purlin system to moment gradient in members due to spatial and directional variation of wind loading are examined. The results from this research lay the foundation for a more accurate design approach that considers the stability of thin-walled structures under spatial and transient wind loading.

1. Introduction

The use of thin-walled structural and cladding materials in construction has been growing over the years. In low-rise buildings, for example, thin walled steel is being utilized in various applications such as in roof systems, wall claddings, roof purlins and trusses, wall girts or as diagonal bracings. With more frequent extreme windstorm events, there is the need to accurately advance knowledge in analysis and design of these thin-walled systems to withstand the spatiotemporal variation of high wind pressure loading.

A number of studies over the years have identified the shortcomings of determination of wind loading from code specified pressure coefficients. Studies conducted by Pierre, Kopp et al. (2005), Coffman, Main et al. (2010) showed that peak bending moments at the knee of a portal frame

¹ Assistant Professor, Civil, Architectural and Environmental Eng., Drexel University, <yaredshi@drexel.edu>

² Graduate Student, Civil, Architectural and Environmental Eng., Drexel University, <khw32@drexel.edu>

³ Associate Professor, Civil and Environmental Eng., Western University, <gbitsuam@uwo.ca>

building computed by using ASCE7-10 (2010) standard plots are mostly less than peak bending moments computed using Database-Assisted Design (DAD), a realistic wind loading analysis technique based on aerodynamic database of wind tunnel tests (Main and Fritz 2006). The study also showed that, even when a good agreement was observed for moment results at the knee, moment results at pinch are significantly underpredicted by ASCE7. Farquhar, Kopp et al. (2005) conducted an experimental test on a simplified standing seam roof under uniform and dynamic wind tunnel uplift pressure. By introducing an external coefficient to relate the failure wind pressure values in the above mentioned two cases, it was found that the design wind load computed using ASCE7 coefficients overestimates the realistic dynamic failure pressure by as much as 30%. Related experimental testing done by Sinno (2008) on a full scale, standing seam roof using suspended magnets to produce electromagnetic uplift pressure revealed a similar outcome with ASCE7 coefficients overpredicting the failure uplift pressure. In addition, the study identified that deflection and deformation in the case of true wind loading case are much higher when compared to uniform uplift pressure case. It was also observed that the failure mode under uniform uplift and true wind loading cases are different. According to (Pierre, Kopp et al. 2005), the inconsistencies that were noticed were attributed to the lower turbulence intensities in the earlier experiments, wind direction being in increments of 45° in earlier experiments compared to 5° increments for DAD and use of much fewer pressure taps for the earlier experiments. In addition, earlier experiments did not consider the effect of frame spacing and properties on the resulting wind loads. Most importantly, the ASCE7 experiments were conducted in the 1970s, a time when there were significant constraints in technology, which led to falling back on simplified methods of computing wind effects thus resulting in significant discrepancies. Enhancement of the ASCE7 standard for the determination of wind loads on buildings can avoid the underestimation of wind effects or the excess cost that occurs due to overestimation of wind effects (Simiu, Letchford et al. 2013).

Current design approaches for cold-formed steel members do not consider the effect of spatial and time variation of wind loading. Furthermore, the available design recommendations for high wind areas for cold-formed steel wall studs and roof purlins use prescriptive methods in the selection and sizing of members and connections (AISI 2015). The spatial variation of wind loading on flanges of walls studs and purlins creates a highly non-uniform moment gradient. Research done by Yu (2005) illustrates that both the elastic and ultimate distortional buckling moments of cold-formed beams are significantly affected by the presence of moment gradient and should not be ignored. In the current study, finite element modeling is used in the evaluation of the stability and strength behavior of trapezoidal thin walled steel roof panel-purlin systems under the action of simulated spatial wind loading. Two single roof panel-purlin systems, representing exterior and interior purlins, are modeled using finite element analysis with pressure coefficients adopted from numerical simulation of wind loading on a low-rise gable roof building. The pressure coefficients are validated using wind tunnel tests done at the Boundary Layer Wind Tunnel Laboratory (BLWTL) of the University of Western Ontario (UWO) (Ho, Surry et al. 2005, Main and Fritz 2006).

2. Wind Tunnel Experiments

A large scope wind tunnel testing on low rise generic building models was conducted at the Boundary Layer Wind Tunnel Laboratory (BLWTL) of the University of Western Ontario (UWO) as part of the windstorm mitigation initiative by the National Institute of Standards and Technology (NIST) and Texas Tech University. The main objective of the testing program was to create a time series wind loading pressure database for low-rise buildings. These recorded pressure-time-series histories are used in the development of the Database-Assisted Design (DAD) technique of

analysis and design of buildings for wind loads, which unlike most wind load provisions, considers the spatial and temporal variation of wind loading. Seven low-rise building models were tested. Variation of wind loading due to parameters such as roof slope, eave height, and building geometry was studied. Models were fitted with pressure tap grids for pressure recording. Turbulence characteristics were created by the use of pneumatically controlled roughness elements of various heights. Additional devices were also used to create turbulence characteristics equivalent with the given length scale of the model. These include spires and barriers near the entrance of the wind tunnel and machine nuts scattered between the roughness blocks and the model. Pressure measurements were taken by using high-speed solid state pressure scanning system. Measurements were taken at 37 wind directions over a 180° range at a 5° increment angle between 270° and 90°. Data was recorded at a sampling frequency of 500Hz for a total sampling duration of 100 seconds. Tests were done for open and suburban exposure with surface roughness coefficient, z_0 , values of 0.03 and 0.3m respectively. The nominal wind tunnel speed at reference height was set at 13 m/s (45 ft/s). ESDU documents have been used as a benchmark to define the wind speed and turbulence intensity profiles in the wind tunnel (ESDU,1974, 1982, 1983). Further information about the wind tunnel experiments and Database-Assisted Design (DAD) can be found in (Ho, Surry et al. 2005, Pierre, Kopp et al. 2005, Main and Fritz 2006, Oh, Kopp et al. 2007).

Pressure coefficient recordings from wind tunnel tests can be converted into pressure time series loads by using Eq.1:

$$P_{\theta_j} = \frac{1}{2} \rho V_H^2 C_{p,\theta_j} \quad (1)$$

where ρ stands for the dry density of air at sea level under standard atmospheric conditions, V_H represents an hourly mean wind speed at roof height and C_{p,θ_j} is the pressure coefficient reading for a given terrain condition and wind direction, θ_j . In general, pressure coefficient readings are referenced to the dynamic pressure at roof height level. However, in order to minimize the effect of high turbulence at roof height, all pressure coefficient readings taken at the UWO wind tunnel were referenced to a dynamic pressure found at a higher height than the roof height of the building. Conversion to reference roof height pressure was done by means of a conversion factor taking into account the ratio of the dynamic pressure at the higher reference location and roof height.

3. Computational Fluid Dynamics Wind Simulation

Innovations in computational fluid dynamics (CFD) and turbulence modeling techniques in recent years offer a new approach for evaluating wind effects on buildings in lieu of wind tunnel studies. Advancements in computing power and availability of numerous CFD software packages have also helped fuel the change. However, validation of CFD analysis results with wind tunnel experiments is essential to give a level of confidence in the results to the practicing engineer.

Previous research done on comparison between CFD and wind tunnel results has shown that CFD produces qualitatively comparable results with wind tunnel results. However, there exist quantitative discrepancies in predicting peak values of wind effects on building structures (Huang, Li et al. 2007, Dagnew, Bitsuamalk et al. 2009, Isam and Simiu 2012). In addition, the dependency of numerical results on grid size, turbulence modeling techniques, computational power among other factors can lead to variations in wind loading predictions. Therefore, it is imperative that

numerical studies are followed by experimental and wind tunnel studies to do a complete assessment of wind effects on building structures.

In the current study, numerical simulation of wind for a low-rise gable roof building is undertaken for a building geometry which is one of the seven low-rise building models tested in the BLWTL at UWO. The building shape and dimension are given in Fig. 1 ($H=18\text{ft.}$, $W=120\text{ft.}$ ($6.67H$), $L=187.5\text{ft.}$ ($10.42H$), $R=5\text{ft}$ ($1:12$ roof slope)). The angle θ in Fig. 1 represents the wind approach angle.

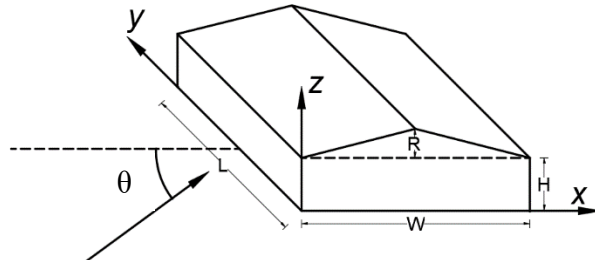


Figure 1 : Building shape and symbol representation for CFD Model

3.1 Computational Domain and Boundary Conditions

The CFD program STARCCM+ is adopted for the wind computational modeling in this study (STARCCM+ 2015). The geometrical modeling of the low-rise building replicates the 1:100 scale model used in the wind tunnel testing for comparison between numerical and wind tunnel results. Geometrical modeling of the flow domain is done using the STAR-CCM+, 3D CAD module. Fig. 2 shows the size of the computational domain defined and the boundary conditions assigned to each face of the flow domain.

Inflow boundary condition is set at $12H$ from the face of the building while a pressure outlet boundary condition is located at $72H$ downstream of the velocity inlet, where H represents the eave height of the building. The vertical extension of the flow domain is set at $10H$ from the no-slip wall ground boundary condition. The lateral extension of the flow domain is set at $16H$ from the center of the building on both sides. The two side walls and the upper boundary of the flow domain are given symmetry plane boundary conditions so as not to provide any improbable blockage to the flow. Finally, the building surface has a no-slip wall boundary condition. For a model scale of 1:100, the total size of the CFD domain will be $72H \times 32H \times 10H$. For the given H of 18 ft., the 1:100 scale flow domain will have a size of $6.1 \times 2.9 \times 0.28$ meters ($19.87 \times 9.6 \times 0.92$ ft.)

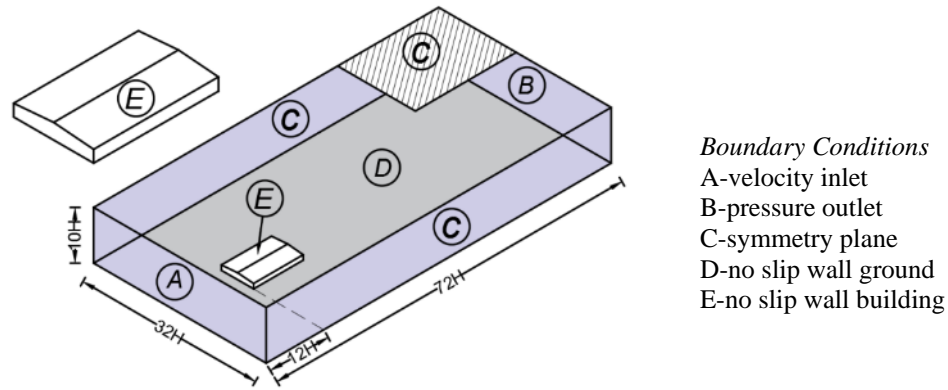


Figure 2: CFD domain and assigned boundary conditions

3.2 Turbulence Modeling

Most CFD software packages use turbulence modeling techniques as an alternative to direct numerical simulation. Among the numerous turbulence models, the Reynolds Averaged Navier Stokes (RANS) and Large Eddy Simulation (LES) are the most widely used (Anderson and Meneveau 2010). Advantages and shortcomings, as well as modifications of these methods for use in flow around bluff bodies, are well documented in (Murakami 1998). LES model with standard and dynamic Sub-Grid Scale (SGS) models were proven to give better agreement with wind tunnel tests for mean pressure coefficient and in capturing vortex shedding properties than RANS models for flow around bluff bodies (Swaddiwudhipong and Khan 2002, Huang, Li et al. 2007, Dagneu, Bitsumalk et al. 2009, Isam and Simiu 2012). For the present study, LES with dynamic SGS model was selected as a turbulence modeling technique for transient simulation and RANS is used for steady state simulation.

It is important to define the correct inflow turbulence boundary condition when using the LES method of turbulence modeling. For the current study, the consistent discrete random inflow generation (CDRFG) method is employed. Proposed by Aboshosha, Elshaer et al. (2015), the CDRFG method is a modification of the discrete random inflow generation (DRFG) method by (Huang, Li et al. 2010). The DRFG method applies a modified random flow generator by (Kraichnan 1970, Smirnov, Shi et al. 2001) to discretize values of power spectra velocities to generate wind fields in each segment. However, inflow turbulent velocities computed using the DRFG method show coherency and spectra discrepancies at low frequency from atmospheric boundary layer (ABL) results. By applying coherency and spectra adjustments to the DRFG, the CDRFG method is capable of matching turbulent velocity results from ABL. Results from (Aboshosha, Elshaer et al. 2015) show that LES with CDRFG inflow turbulence modeling technique produce flow properties and building responses that show good matching with results from similar wind tunnel studies. As an input for the CDRFG method, velocity and turbulence intensity profiles from the UWO wind tunnel test were used. The turbulent velocity field for the along wind direction and an open exposure is shown in Fig. 3.

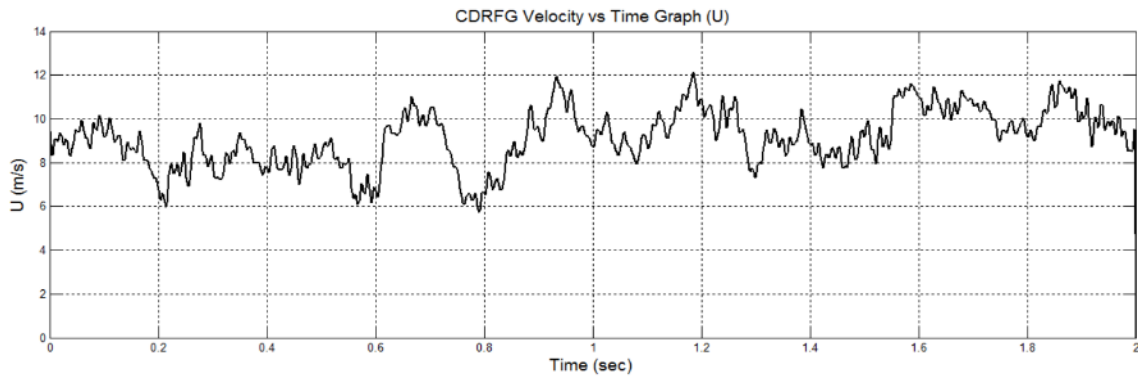


Figure 3: CDRFG turbulent velocity vs time plot for along wind direction

3.3 Flow Domain Discretization

The flow domain was discretized using a polyhedral type of mesh. Prism layer meshes are used near the ‘no slip wall’ boundaries of the low-rise building and the bottom face of the flow domain. Prism layer meshes are high aspect ratio cells which have the advantage of reducing the stream wise discretization while helping the solver give precise near wall flow results. In addition, prism layers are known in satisfying the Y^+ requirement in the viscous sublayer of a turbulent flow. Care is taken to avoid highly skewed prism layer meshes around the sharp corners of the building. Mesh size distribution is done in such a way to have finer meshes in key locations such as around the building, the wake flow region, and the region between the inlet boundary and the front face of the building. Two mesh continuums, Mesh-1 and Mesh-2 were created to check the dependency of the results to mesh size distribution. Mesh-1 and Mesh-2 continuums contained more than 730,000 and 2,900,000 cells respectively. Fig. 4 shows the Mesh-2 continuum adopted in the CFD simulation.

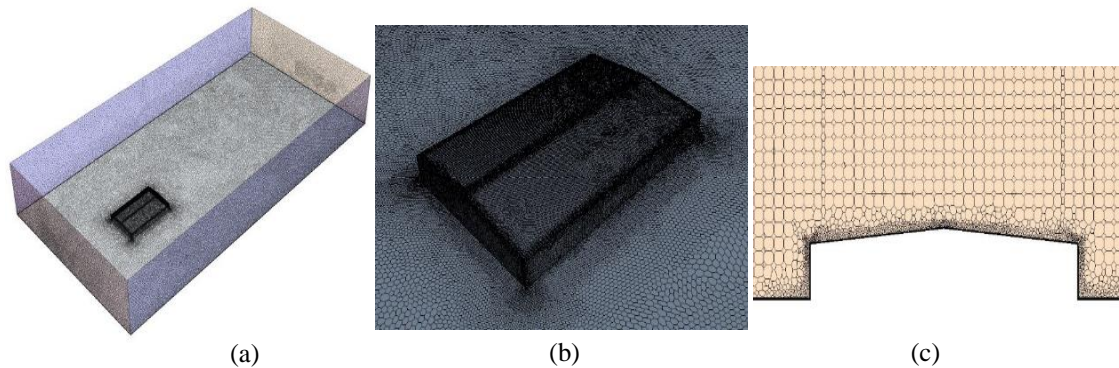


Figure 4: Mesh continuum adopted for CFD simulation (a) 3d view (b) mesh refinement near building (c) section view of prism layer mesh near building surface

3.4 CFD Simulation Results

A total of six simulations, three wind approach angles (0° , 45° & 90°) and two mesh continuums, were completed. The simulations were conducted on the Proteus computer cluster which is part of the University Research Computing Facility (URCF) at Drexel University. All simulations were done for a time step of 0.0002 seconds with a total simulation running time of 8 seconds. At each time step, an inner iteration criterion of 10 iterations was set. These resulted in a total of 40,000 time steps and 400,000 iterations. A solution history file including time step recordings of the

velocity vector and pressure coefficient was created and updated for post processing. It should be noted that solution history recording for only the last 2 seconds of the simulations is used in the generation of pressure coefficients to guarantee the convergence of the flow.

An initial steady state simulation for the three wind approach angles showed that the 90° approach angle resulted in the largest flow separation zone which directly correlates with a wide negative pressure zone on the roof of the low-rise building. In the other two cases, the resulting negative pressure zone was confined to a small area of the roof. Fig 5 shows the associated pressure coefficient contour plots for the three wind approach angles under consideration. Even though peak pressure coefficient zones for the 0° and 45° cases are greater than the 90° case, the latter case gives a gradually varying and wider negative pressure zone.

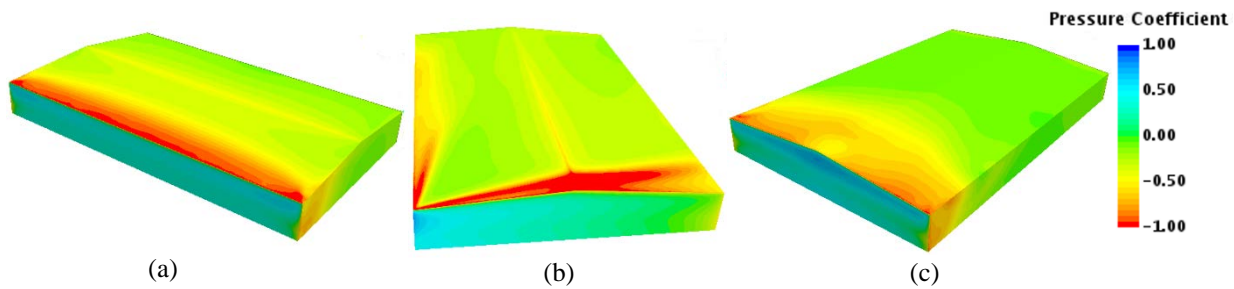


Figure 5: Pressure Coefficient Contour Plot for Different Wind Approach Angle: (a) 0° (b) 45° (c) 90°

3.5 Validation with UWO Wind Tunnel Data

The results of the CFD simulations are validated with wind tunnel testing done on similar building model at the University of Western Ontario (UWO). Fig. 6 shows the mean C_p contour plots on the roof of the model building in question for the 90° wind approach angle. The overall spatial distribution of pressure shows a similar trend in both the CFD and wind tunnel results. Using numerical simulation, the spatial distribution of wind pressure was successfully replicated for all wind approach angles considered. Fig. 7 shows mean pressure coefficient variation along the length of the roof of the low-rise building at $0.5H$ from the right edge of the building. The comparison for the 45° and 90° wind directions show excellent agreement at all points along the line. Numerical simulation is observed to overpredict the mean pressure coefficient for roof length beyond $3.5H$. For the 0° wind direction, while the trend for both numerical simulation and wind tunnel are the same, the former one results in mean pressure values about 20% higher than the latter.

Comparison is also made for point-based transient pressure coefficient recordings over the roof of the low-rise building for the 90° wind approach angle. Four pressure taps on the roof of the low-rise building that are representative of the overall distribution of the negative pressure are selected to check the validity of the point-based pressure coefficient recordings over time. The locations of the four pressure taps are indicated in Fig. 8. The 2-second numerical simulation pressure coefficient is compared with (1) the full 100-second wind tunnel recording and (2) an average of 5 randomly selected 2-second subset wind tunnel recordings. A summary of the statistical comparison between the wind tunnel and numerical simulation results is shown in Table 1. The comparisons show that mean values for pressure taps 1603 and 3704 compare within a reasonable range. These taps represent the high flow separation zone near the windward edge of the roof. Comparison for the remaining two taps under consideration show a higher disparity in pressure

coefficient readings. This is also evident in the mean pressure coefficient contour plots (Fig. 6) with a rapid drop of mean pressure coefficient observed along the length of the roof in contrast to a smooth transition for wind tunnel and numerical results respectively. This can be attributed to the higher turbulence intensity in the case of the wind tunnel testing.

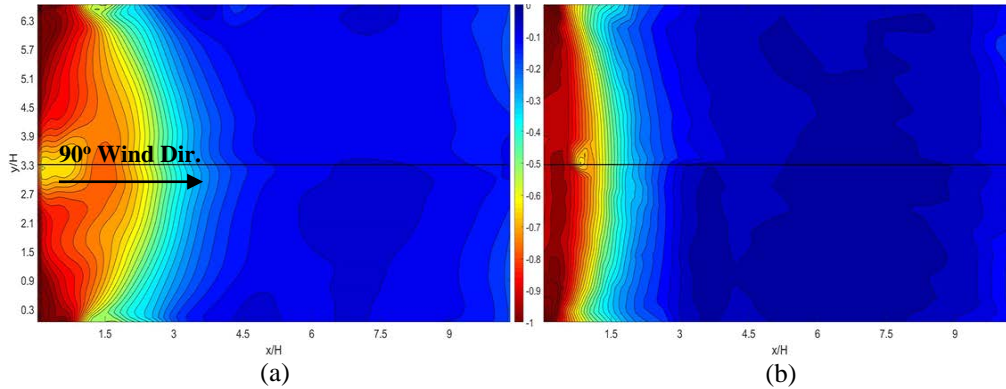


Figure 6: C_p Distribution comparison for 90° wind approach (a) CFD (b) UWO Wind Tunnel

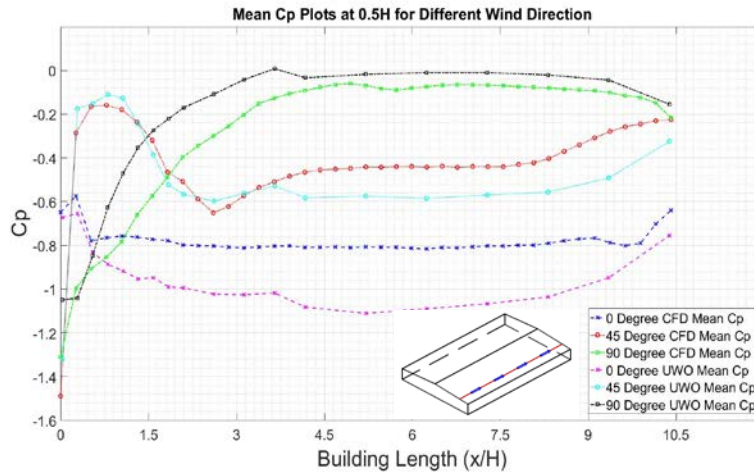


Figure 7: Comparison between numerical simulation and wind tunnel along building roof length

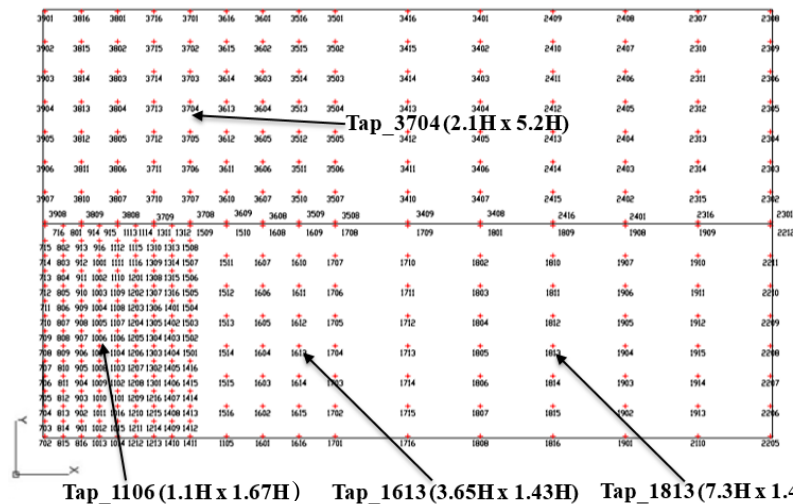


Figure 8: UWO wind tunnel testing pressure tap layout and XY coordinates over the roof of the low-rise building

Table 1: Point based CFD and UWO wind tunnel C_p comparison

Tap #	Max -ve C_p		Mean C_p		St. Div.		Max -ve C_p		Mean C_p		St. Div.	
	UWO (100s)	CFD (2s)										
1106	-2.376	-1.85	-0.664	-0.754	0.286	0.323	-2.376	-1.85	-0.664	-0.754	0.286	0.323
1613	-1.041	-0.494	0.003	-0.119	0.11	0.073	-1.041	-0.494	0.003	-0.119	0.11	0.073
1813	-0.452	-0.27	-0.005	-0.102	0.082	0.038	-0.452	-0.27	-0.005	-0.102	0.082	0.038
3704	-2.65	-0.626	-0.199	-0.214	0.172	0.107	-2.65	-0.626	-0.199	-0.214	0.172	0.107

3.6 Effect of Wind Directionality on Panel-purlin System

The test panel under investigation is assumed to be part of the roof envelope of the model building. It is located at the right front edge of the building envelope (Fig. 9). Using the method of tributary area implemented by NIST’s aerodynamic Database-Assisted Design (DAD) software for wind, the test panel is divided into pressure loading zones that create the spatial variation of pressure. The size of the test panel, pressure tap tributary area, and mean pressure coefficients are shown in Fig 10. For a given pressure tap tributary area, the spatial variation of pressure is assumed to be zero. However, the restriction on the number of pressure taps that can be fit on a model scale of a low-rise building could mean the tributary area for a given pressure tap is very large directly affecting the spatial variation of pressure on a roof panel. This restriction was apparent in this study as only six pressure tap readings were accommodated on both exterior and interior panel-purlin systems which represent a total roof area of 27 and 45 ft² respectively. By using pressure coefficient data from numerical simulation results, the restriction on the number of pressure taps can be avoided, giving the ability to create sufficient spatial distribution of wind pressure. By increasing the number of pressure taps and limiting the maximum tributary area of a tap to 1 ft², a well-defined spatial pressure distribution is achieved.

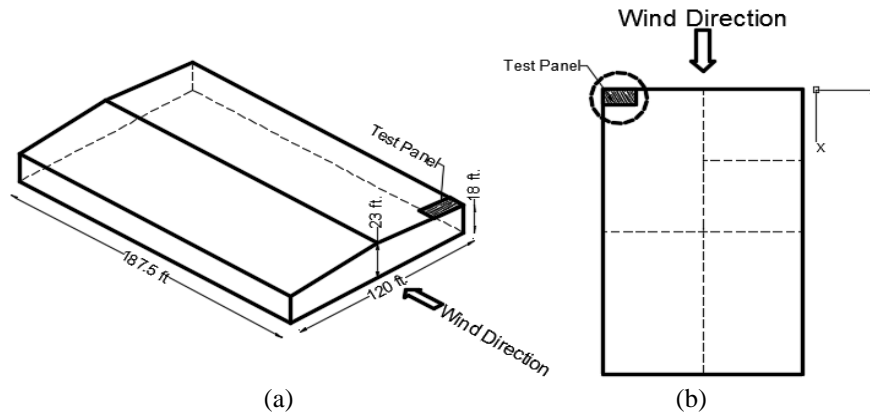


Figure 9: Test Panel Location (a) 3d building view (b) Top roof view

Using numerical simulation results the number of pressure taps is increased to 200. Mean pressure coefficient results are extracted from the numerical simulation for the three wind approach angles considered. For the given test panel location, Fig. 11 shows the spatial variation of wind loading for the different wind approach angles. All the three wind angles produced unique wind pressure distribution. A well-defined two-way variation can be seen for 45° wind approach angle. The 45°

angle also gives higher pressure coefficient values compared with the remaining two. On the other hand, the 0° wind approach angle exhibits a rather one-dimensional wind pressure distribution with a fairly uniform wind pressure loading along purlin lines. The 90° wind approach angle also produces a fairly uniform wind pressure distribution in both directions. However, magnitudes of pressure coefficient values are higher in this case.

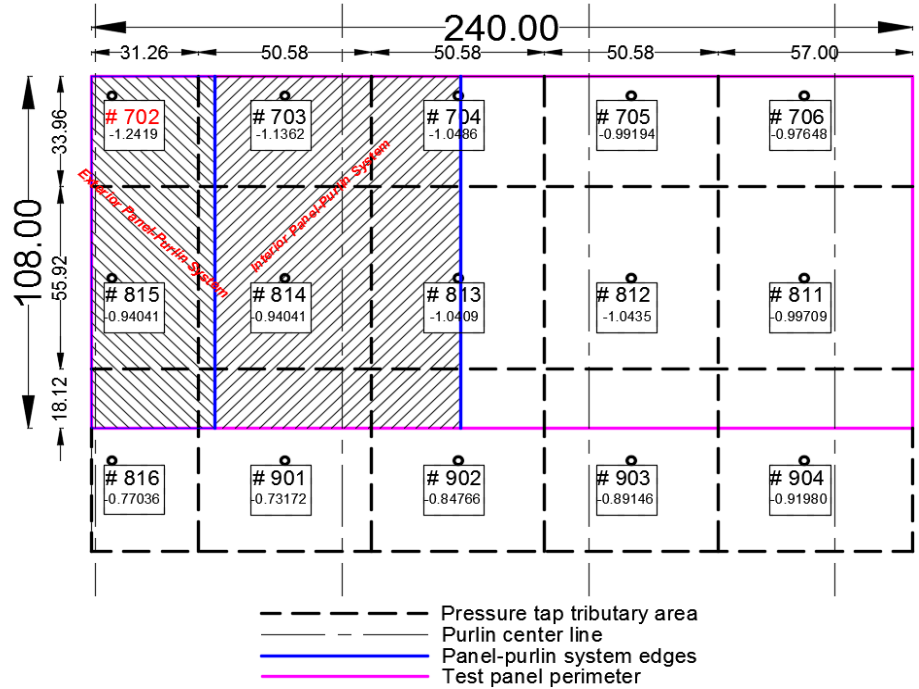


Figure 10: Panel-purlin system test setup, pressure tap layout and mean pressure coefficients

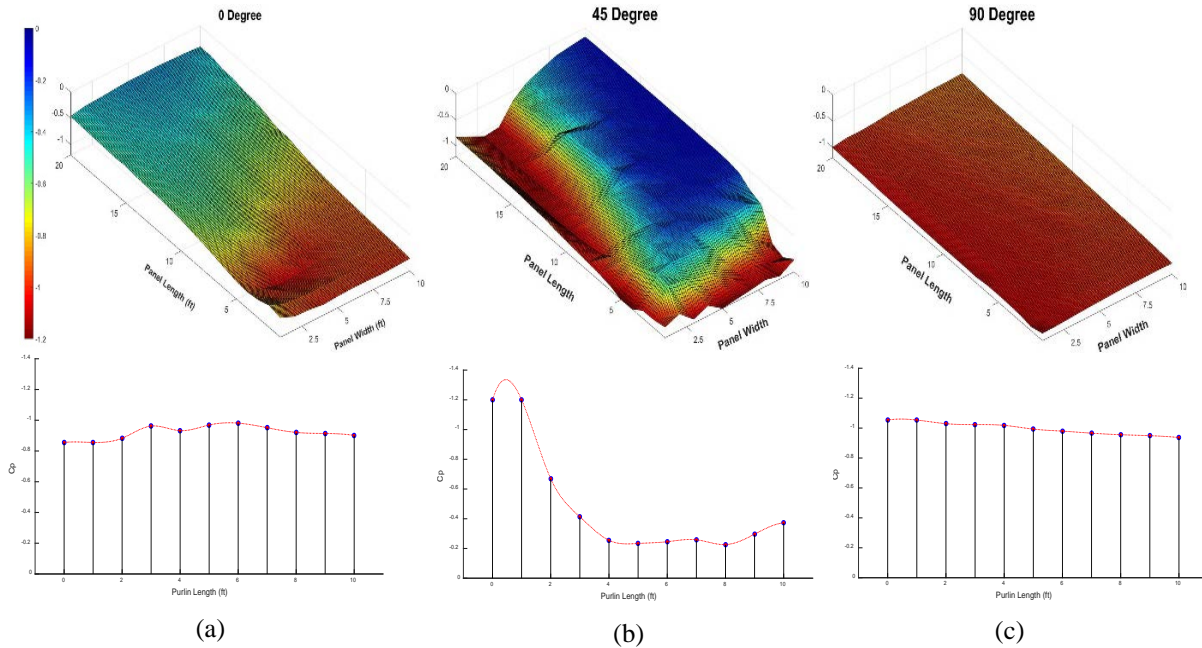


Figure 11: Mean pressure coefficient distribution over test panel surface and purlin line at $x=5\text{ft}$. (a) 0° (b) 45° (c) 90°

4. Finite Element Analysis

4.1 Development of Single Roof-purlin System Finite Element Model

Two single trapezoidal roof panel-purlin systems (windward exterior and interior), part of the low-rise building envelope, are selected for examining the structural response. A 9.5Z2.25x105 standard Z-section purlin, with height, width and thickness of 9.5x2.25x0.105 inches, and a 22-gauge trapezoidal PBR roof panel (width of 108 in.) by CECO Metal Building Systems with a thickness of 0.0299 inches are selected for the analysis. Fig. 12 shows the components of the roof panel purlin systems and key dimensions for the trapezoidal panel considered.

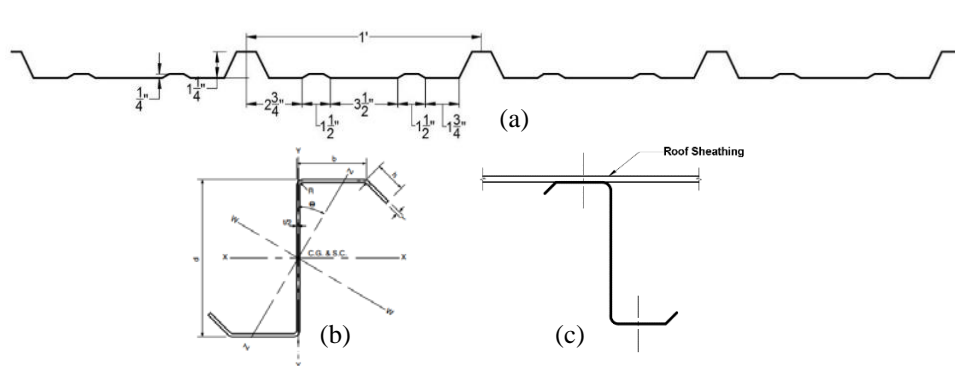


Figure 12: Roof panel-purlin system components (a) Trapezoidal roof panel (b) Z-purlin section (c) panel-purlin system

4.2 Finite Element Modeling

4.2.1 Material Modeling

In both panel and purlin sections, cold-formed steel with elastic modulus of 29500 ksi, Poisson's ratio of 0.3, yield stress of 33ksi, where the true stress and true strain material model shown in Fig. 13 is adopted.

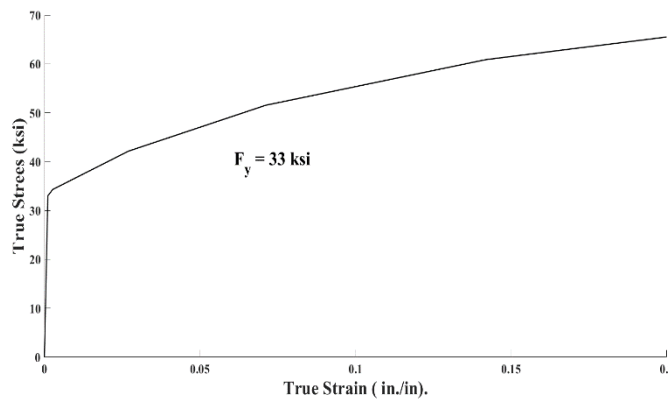


Figure 13: True Stress-Strain model for FE analysis

4.2.2 Meshing and Element Type

Computational modeling and meshing of the roof panel-purlin system is done by incorporating CAD, finite strip (CUFSM) and finite element (ABAQUS) tools. S4R shell elements were used to represent the computational model for both the roof panel and purlin. S4R shell elements are general purpose conventional shell elements with 4 node, quadrilateral, reduced integration and large strain formulation that can be used in three-dimensional stress analysis (ABAQUS 2013).

Meshing was done by employing dissimilar seeding sizes along the two principal axes in both the panel and purlin cases. In the case of the roof panel, mesh sizes were more refined across the width of the roof panel, while a coarser mesh seeding is used along the length. Similar meshing configuration was also used for purlins.

4.2.3 Boundary Conditions

One of the main challenges of setting up the panel-purlin system finite element model lies in the modeling of the fastener connection behavior under wind loading with failure commonly occurring due to pull-through or tearing of panel material from the attachment point (Lu, Makelainen et al. 2008, Fan, Rondal et al. 1997, Mahaarachchi and Mahendran 2004). The simplest way of modeling fasteners is by assigning a pinned support condition which is fixed in translation but able to rotate in all the three principal axes, an approach used to study the effect of point load location on trapezoidal roof cladding systems and steel cladding pull-through failures under wind loading (Mahaarachchi and Mahendran 2004, Majid, Muhammad et al. 2014). In the case where there is experimental data on the load-displacement relationship to characterize the stress-strain properties of a fastener, fasteners can be modeled as springs with equivalent linear and rotational stiffness values (El Damatty, Rahman et al. 2003).

In the current study, multi-point linear constraint equations are used to define connections between panel and purlin. Multi-point constraints define the relative motion of nodes by equating the linear combination of nodal outputs to zero (ABAQUS 2013). The general form of the algorithm is given in Eq. 2.

$$A_1 u_i^P + A_2 u_j^Q + \dots + A_n u_k^R = 0 \quad (2)$$

where $A_1 u_i^P$ represents a nodal variable at node p , degree of freedom i . A_n variables represent coefficients used to define relative motion between connected nodes. Adjacent nodes on panel and purlins are connected using a similar approach. Fasteners are located at every other crest in the traverse direction, representing a spacing of 2ft. Relative displacement between adjacent fastener nodes on panel and purlins is set to 0. Other degrees of freedom are not restrained. The general form of the equation is given in Eq. 3.

$$1u_2^{Panel\ node} + 1u_2^{purlin\ node} = 0 \quad (3)$$

Free edges of roof panels are left free while cut sections are assigned appropriate symmetry boundary conditions with translation along symmetry plane and rotation along perpendicular axes set to zero. Displacement in axis 2 and 3 are fixed at the two ends of the purlin. A single node at one end of the bottom flange of the purlin is fixed from displacement in the longitudinal 1-direction. The final mesh and boundary condition configuration for both the interior and exterior panel purlin systems is given in Fig. 14.

4.3 Stability of Panel-purlin System under Wind Loading

Suction pressure loading is applied to the surface of the test panels according to the pressure tap layout and numerically computed pressure coefficients. The general process involves identifying the nodes, elements, and surfaces associated with each pressure tap's tributary area and applying the spatial pressure on each surface. The panel is also tested under uniformly distributed negative

pressure loading computed using the ASCE-7-10 provision to study the behavior of panel-purlin systems under the currently prescribed wind loading standards. The analysis would also help in determining the peak wind speed that causes instability and collapse under static wind loading conditions.

Elastic buckling analysis of edge and intermediate single roof panel-purlin systems under uniform and spatial non-uniform loading cases are considered where the effect of wind directionality on the stability of roof panel purlin systems is examined by considering 0° , 45° and 90° wind direction mean pressure coefficients. Two distinct types of buckling modes are observed. Buckling is initiated at the region of the panel with higher pressure coefficient. This corresponds to the edge of the panel with free boundary condition for 0° and 90° directions. For the 45° wind direction case, a wider high-pressure zone is found away from the free edge. Fig. 15 illustrates the buckling shapes of the panel under the different loading conditions.

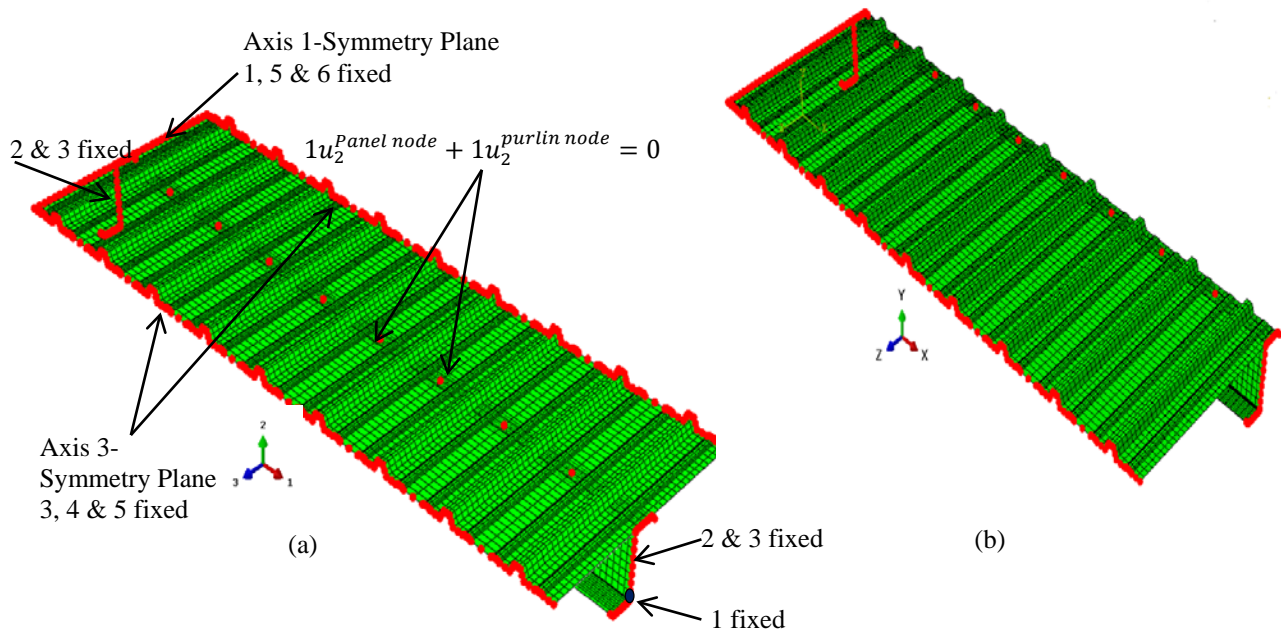


Figure 14: Finite element model and boundary conditions for (a) interior (b) exterior panel-purlin

Critical equivalent wind speeds causing instability of panel purlin systems are computed and compared with uniform wind loading case. Basic wind speeds in ASCE7-10 are given as 3-second gust speeds measured at 10m above the ground for an open terrain condition. On the other hand, pressure coefficients for numerical and wind tunnel simulations are normalized using wind speeds at roof height and with an averaging time of 1hr (Main and Fritz 2006). To convert hourly mean wind speeds associated with non-uniform pressure loading to the equivalent 3-second gust wind velocity, the Durst Curve is used (ASCE7-10). Table 2 summarizes the results of panel purlin system stability. The results show that stability of panel-purlin systems is highly dependent on wind direction that would, in turn, govern the spatial variation of wind pressure. Edge panel-purlin systems also tend to become unstable under reduced wind speeds compared to interior systems. This is due to the higher magnitude of pressure coefficients near the windward edge of the building. In all cases, uniform wind loading conditions are found to be over conservative with buckling wind speeds from non-uniform wind loading cases being on average 25% greater.

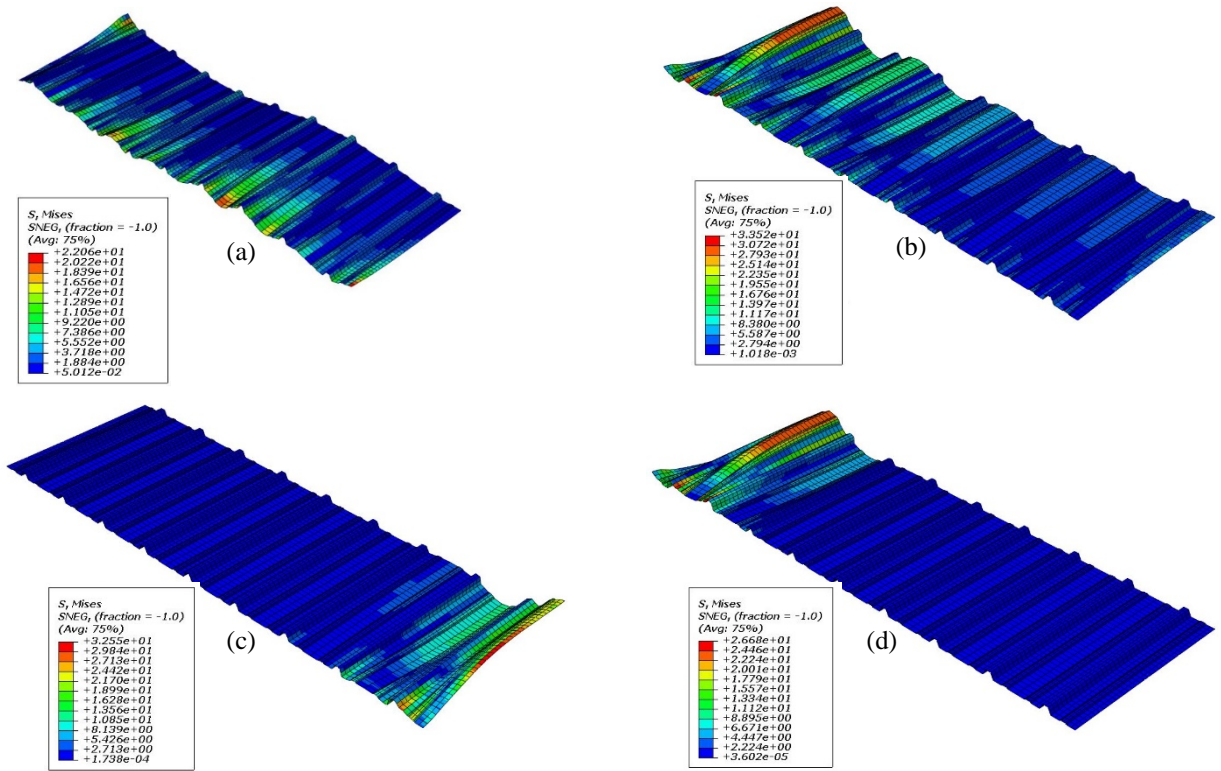


Figure 15: First buckling modes for edge roof panel-purlin system a) uniform wind loading b) 0° wind direction c) 45° wind direction d) 90° wind direction

Table 2: Stability analysis results for panel-purlin systems under uniform and non-uniform wind loading

FE	Panel-Purlin System Type	Wind Loading Type	Wind Dir. (degrees)	$P_{buck,max}$ (psf)	V_{buck} mph (hourly)	$\frac{V_{buck,non-uniform}}{V_{buck,uniform}}$
1	Edge	N-Uniform	0	-11.02	65.9	1.55
2	Edge	N-Uniform	45	-13.43	66.3	1.25
3	Edge	N-Uniform	90	-10.08	59.4	1.12
4	Interior	N-Uniform	0	-19.49	85.5	1.30
5	Interior	N-Uniform	45	-17.66	75.8	1.15
6	Interior	N-Uniform	90	-15.48	74.7	1.13
7	Edge	Uniform	-	-9.64	52.9	-
8	Interior	Uniform	-	-15.02	66.0	-

Elastic buckling analysis of the purlin Z section is done where 0° , 45° and 90° wind direction mean pressure coefficients are considered in addition to a uniform wind loading case. For all cases considered, the application of load at the top flange initiates distortional buckling modes at regions of maximum loading. For uniform, 0° and 90° wind loading cases, a minimal spatial variation of wind exists and distortional buckling modes are observed. Furthermore, observed modes include twisting along the longitudinal axis due to the unsymmetrical flange loading, as well as local buckling at the unstiffened top flange lip that propagates to the adjacent flange. Summary of the

Eigen analysis results for the first distortional buckling modes and associated moment gradients between the ends of the purlin is given in Table 3. The results of the stability analysis show reduced distortional buckling capacity in the case of flange-loaded purlins under non-uniform wind conditions. In terms of moment gradient, the 45^0 wind direction creates the highest gradient. However, all cases produce moment gradients that are characterized by a single curvature as indicated by the negative sign of the moment gradient. The reduced distortional buckling moment could be due to the location of loading as well as the non-uniformity of the load. Since the load is applied to the top flange, the whole section of the member would not be active in resisting the applied loading giving little resistance to buckling. The top flange is mostly acting as a plate stiffened on one side by the connection to the web. Fig. 16 shows typical buckling mode shapes observed.

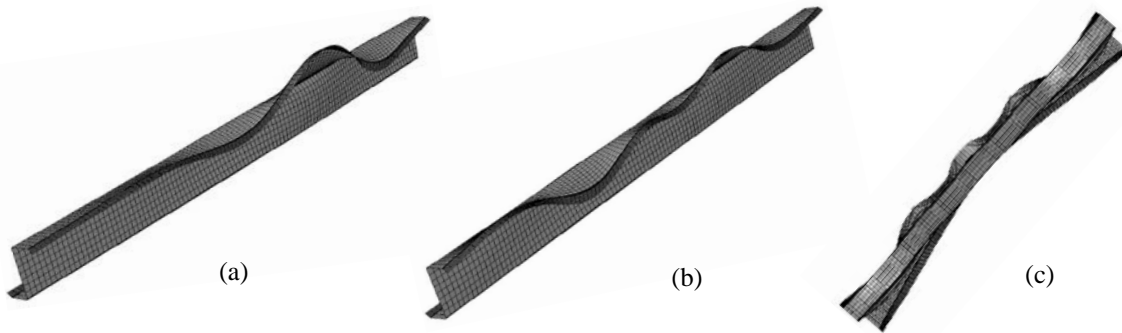


Figure 16: Observed buckling mode shapes a) 45^0 unsymmetrical distortional buckling b) 0^0 anti-symmetric distortional buckling c) Global-local interaction

Table 3: Distortional buckling in edge and intermediate purlins

Purlin Type	Loading Case	Moment Gradient (M_2/M_1)	f_y (ksi)	M_y (kip-in)	M_{crd}^1 (kip-in)	M_{crd-MG}^2 (kip-in)
Edge Purlin	0	-1.00	33	134.6	314.9	157.94
Edge Purlin	45	-0.97	33	134.6	314.9	158.48
Edge Purlin	90	-0.98	33	134.6	314.9	-159.16
Intermediate Purlin	0	-0.97	33	134.6	314.9	159.60
Intermediate Purlin	45	-0.69	33	134.6	314.9	-188.79
Intermediate Purlin	90	-0.98	33	134.6	314.9	-159.37

1. M_{crd} --- elastic distortional buckling moment under constant moment
2. M_{crd-MG} --- elastic distortional buckling moment under flange load and moment gradient

4.4 Collapse Analysis of Panel-purlin System under Wind Loading

Collapse analysis of single roof panel-purlin systems was conducted to determine critical wind speeds leading to cladding failure. For an edge panel-purlin system, collapse behavior under the impact of uniform and non-uniform wind loading, and wind directionality is carried out by the modified RIKS method, a non-linear static analysis method (ABAQUS 2013). Geometrical nonlinearity is introduced based on an Eigen buckling mode shape with an imperfection amplitude of $L/2000$. In all cases considered, material yielding is concentrated near fastener locations; similar observations were made in the pull-through failures at fastener locations due to transverse fracture as observed by Mahaarachichi (2003), while panel regions away from fasteners remain elastic. Uniform wind loading causes symmetrical deformation between each fastener, whereas deformations due to non-uniform loading conditions are more localized around the free edge of

the panel (Fig. 17) For all non-uniform wind loading cases, maximum deflection is observed at first interior panel crest mid-point from the free edge of the panel indicating the impact of member continuity and boundary conditions.

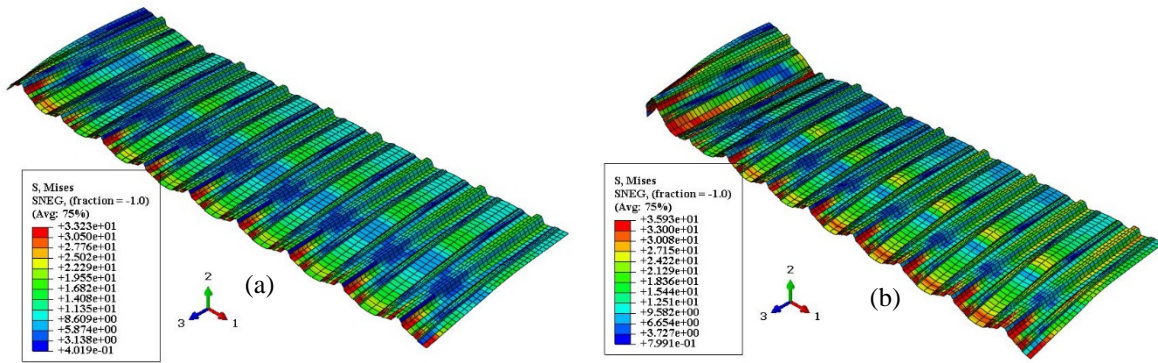


Figure 17: Deformation at collapse with stress contour a) Uniform wind loading b) 45° wind direction

Collapse behavior of thin-walled steel purlins under realistic wind loading is carried out by the modified RIKS method with initial and maximum time increment sizes are set to 0.001 and 0.1 respectively, and a maximum number of increments equal to 200 (Yu 2005, Moen 2009, Shifferaw 2012). The magnitude of maximum initial imperfections for local and distortional imperfections is determined by using cumulative distribution functions (CDF) values which indicate the probability of selected imperfection value exceeding maximum imperfection in a typical member (Schafer and Peköz 1998). In this study, maximum imperfection values based on 75% CDF is used. Maximum global imperfection magnitude is set at $L/2000$. Collapse is initiated by outward buckling of the top flange, followed by formation of local dents on the web close to the midpoint due to twist, with collapse mechanism achieved by an excessive twist that propagates to the lower compression flange. For uniform, 0° and 90° wind loading cases, the maximum deformation occurs around the midpoint. The maximum deformation location shifts to the point of maximum loading for 45° wind loading case (Fig. 18). Fig. 19 shows load displacement plot for the non-uniform loading conditions indicating that the 45° wind direction produces the highest ultimate strength due to the high moment gradient (M_{ud-MG}) developed by the wind directionality in that case.

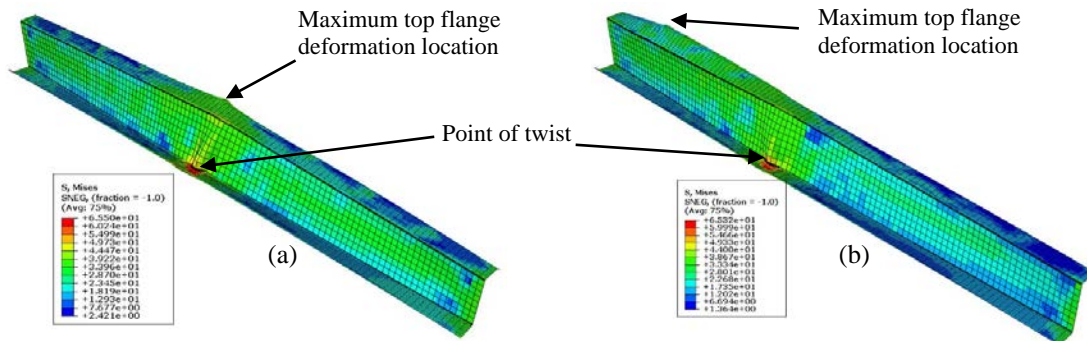


Figure 18: Collapse of purlin member for a) uniform, 0° , and 90° b) 45°

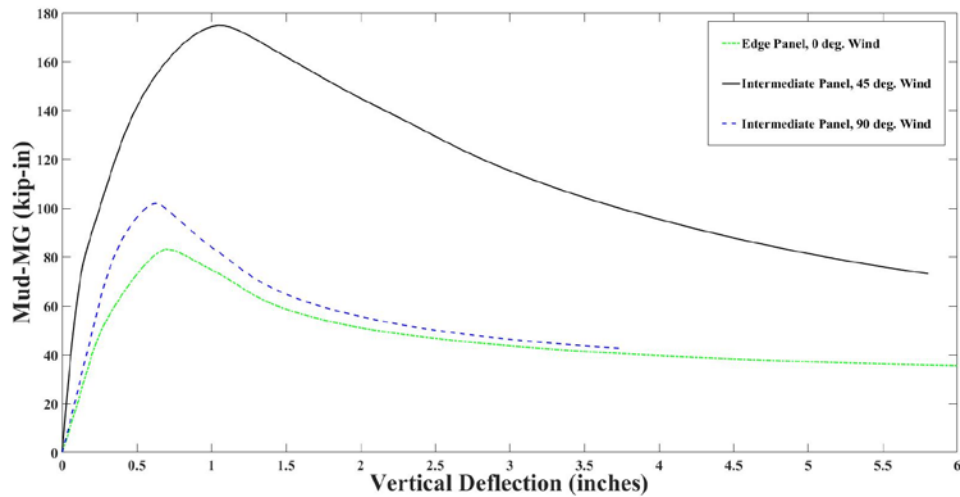


Figure 19: Load-displacement curve for roof purlin members under wind loading

5. Conclusions

The stability and collapse behavior of a thin-walled building cladding and component systems under the action of spatially varying wind loading are examined. Steady state simulation of wind on a low-rise metal building for 0° , 45° and 90° wind directions is undertaken through computational fluid mechanics. Existing wind tunnel tests are used to validate the numerical simulation results. The lack of restriction in data points for reading flow properties makes the numerical analysis for wind loading evaluation a critical tool in the study of stability and strength of the roof panel-purlin system and purlin member under spatial and time-varying wind loading cases. Critical wind speeds related to the panel-purlin system instability and collapse are computed and related to wind direction, maximum uplift pressure and deflections. Wind direction and associated pressure distribution are found to play an important role in the stability and strength of the thin-walled structural systems. Examination of the purlin, acted upon by a non-uniform wind load at the top flange, reveals the prevalence of distortional buckling modes as well as local-global interaction with wind direction influencing how buckling waves propagate along the length of the member. Non-uniform spatial variation of wind loading cases creates moment gradient effect impacting the strength and stability behavior of the thin-walled roof purlin members.

Future research effort would focus on comprehensive validation of the numerical CFD and FE analyses for aerodynamic and structural responses with experimental testing specific to thin-walled structures. Finite element model refinement is required in modeling connection elements and fracture around fastener locations. Further work needs to address the incorporation of wind pressure recordings from additional wind directions and building shapes, as well as an examination of stability under transient wind loading in which CFD can be used to generate such transient wind pressure data as shown in Fig. 20. The research work undertaken demonstrated the potential feasibility of numerical analysis methods in predicting and utilizing spatially varying wind pressure loading in cladding and component members' stability and strength determination. This lays the foundation for the development of a more accurate analysis and design approach in improving wind hazard mitigation of thin-walled structures under spatiotemporal variation of extreme wind effects.

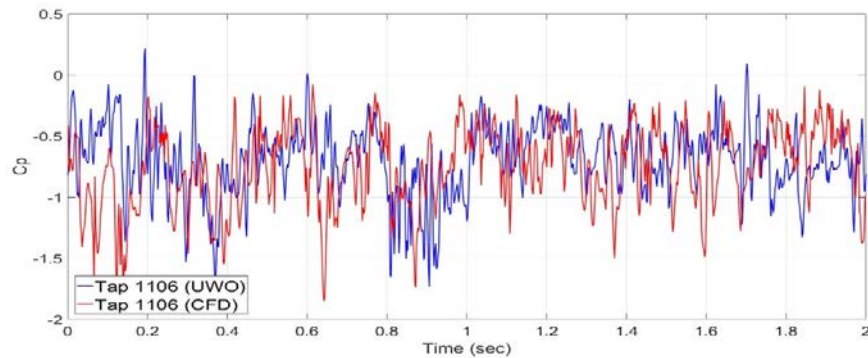


Figure 20: Transient pressure coefficient comparison for wind tunnel and CFD

Acknowledgments

The authors would like to acknowledge Tibebu Birhane of University of Western Ontario for the invaluable support in the computational fluid dynamics modeling of this work.

References

- ABAQUS (2013). ABAQUS/Standard Version 6.13-1. Providence, RI, Dassault-Systems.
- Aboshosha, H., A. Elshaer, G. T. Bitsuamlak and A. El Damatty (2015). "Consistent inflow turbulence generator for LES evaluation of wind-induced responses for tall buildings." *Journal of Wind Engineering and Industrial Aerodynamics*, 142: 198-216.
- AISI-S230-15 (2015). "Standard for Cold-formed Steel Framing-Prescriptive method for one- and two-family dwellings." *American Iron and Steel Institute*, Washington, D.C.
- Ali, H. M. and P. E. Senseny (2003). "Models for standing seam roofs." *Journal of Wind Engineering and Industrial Aerodynamics*, 91(12–15): 1689-1702.
- Anderson, W. and C. Meneveau (2010). "A large-eddy simulation model for boundary-layer flow over surfaces with horizontally resolved but vertically unresolved roughness elements." *Boundary-Layer Meteorology*, 137: 397.
- ASCE7-10 (2010). "Minimum design loads for buildings and other structures." *American Society of Civil Engineers*, Reston, VA.
- Coffman, B. F., J. A. Main, D. Duthinh and E. Simiu (2010). "Wind Effects on Low-Rise Metal Buildings: Database-Assisted Design versus ASCE 7-05 Standard Estimates." *Journal of Structural Engineering*, 136(6): 744-748.
- Dagnew, A. K., G. T. Bitsuamalk and R. Merrick (2009). Computational Evaluation of Wind Pressure on Tall Buildings. *11th American Conference on Wind Engineering*, San Juan, Puerto Rico.
- El Damatty, A. A., M. Rahman and O. Ragheb (2003). "Component testing and finite element modeling of standing seam roofs." *Thin-Walled Structures*, 41(11): 1053-1072.
- Engineering Sciences Data Unit (ESDU) (1983). Strong winds in the atmosphere boundary layer. Part 2: Discrete gust speeds. Data Item 83045.
- Engineering Science Data Unit (ESDU) (1974). Characteristics of atmospheric turbulence near the ground. Data Item 74031.
- Engineering Sciences Data Unit (ESDU) (1982). Strong winds in the atmosphere boundary layer. Part 1: Mean-hourly wind speeds. Data Item 82026.
- Fan, L., J. Rondal and S. Cescotto (1997). "Finite element modelling of single lap screw connections in steel sheeting under static shear." *Thin-Walled Structures*, 27(2): 165-185.
- Farquhar, S., G. A. Kopp and D. Surry (2005). "Wind tunnel and uniform pressure tests of a standing seam metal roof model." *Journal of structural engineering*, 131(4): 650-659.
- Ho, T. C. E., D. Surry, D. Morrish and G. A. Kopp (2005). "The UWO contribution to the NIST aerodynamic database for wind loads on low buildings: Part 1. Archiving format and basic aerodynamic data." *Journal of Wind Engineering and Industrial Aerodynamics*, 93(1): 1-30.
- Huang, S., Q. S. Li and S. Xu (2007). "Numerical evaluation of wind effects on a tall steel building by CFD." *Journal of Constructional Steel Research*, 63(5): 612-627.
- Huang, S. H., Q. S. Li and J. R. Wu (2010). "A general inflow turbulence generator for large eddy simulation." *Journal of Wind Engineering and Industrial Aerodynamics*, 98(10–11): 600-617.

- Isam, J. and E. Simiu (2012). "Large Eddy Simulation of Wind Loads on a Low-Rise Structure and Comparison with Wind Tunnel Results." *Applied Mechanics and Materials*, 152-154: 8.
- Kraichnan, R. H. (1970). "Diffusion by a Random Velocity Field." *Physics of Fluids*, 13(1): 22.
- Lu, W., P. Makelainen and J. Outinen (2008). "Finite Element Modeling of Single Lap Shear Screw Connection in Steel Sheeting in Fire." *The open construction & building technology journal*, 2(1): 257-261.
- Mahaarachchi, D. and M. Mahendran (2004). "Finite element analysis and design of crest-fixed trapezoidal steel claddings with wide pans subject to pull-through failures." *Engineering Structures*, 26(11): 1547-1559.
- Main, J. A. and W. P. Fritz (2006). Database-assisted design for wind: concepts, software, and examples for rigid and flexible buildings. Gaithersburg, MD U.S. Department of Commerce, Technology Administration, National Institute of Standards and Technology.
- Majid, T., M. Muhammad, N. I. Ramli, C. D. SNA, W. C. FA and N. Marcus (2014). "Behaviour of Trapezoidal Roof Cladding under Different Location of Point Load." *Journal of Civil Engineering Research*, 4(3A): 149-153.
- Murakami, S. (1998). "Overview of turbulence models applied in CWE-1997." *Journal of Wind Engineering and Industrial Aerodynamics*, 74-76(0): 1-24.
- Oh, J. H., G. A. Kopp and D. R. Incullet (2007). "The UWO contribution to the NIST aerodynamic database for wind loads on low buildings: Part 3. Internal pressures." *Journal of Wind Engineering and Industrial Aerodynamics*, 95(8): 755-779.
- Pierre, L. M. S., G. A. Kopp, D. Surry and T. C. E. Ho (2005). "The UWO contribution to the NIST aerodynamic database for wind loads on low buildings: Part 2. Comparison of data with wind load provisions." *Journal of Wind Engineering and Industrial Aerodynamics*, 93(1): 31-59.
- Shifferaw, Y., Schafer, B. (2012). "Inelastic bending capacity of cold-formed steel members." *Journal of Structural Engineering*, 138(4), 468-480.
- Simiu, E., C. Letchford, A. G. Chowdhury, D. Yeo and N. Isyumov (2013). "Assessment of ASCE 7-10 Standard Methods for Determining Wind Loads." *Journal of Structural Engineering*, 139(11): 2044-2047.
- Sinno, R. R. (2008). Response of Metal Roofs to Uniform Static and True Hurricane Wind Loads. *International Speciality Conference on Cold-Formed Steel Structures*.
- Smirnov, A., S. Shi and I. Celik (2001). "Random flow generation technique for Large Eddy Simulations and particle-dynamics modeling." *Journal of fluids engineering-Transaction of the ASME*, 123(2): 359-371.
- STARCCM+ (2015). STARCCM+ solver. Detroit, MI, CD-adapco.
- Swaddiwudhipong, S. and M. S. Khan (2002). "Dynamic response of wind-excited building using CFD." *Journal of Sound and Vibration*, 253(4): 735-754.
- Yu, C. (2005). Distortional Buckling of Cold-Formed Steel Members in Bending, Johns Hopkins University.